JACS
JOURNAL OF THE AMERICAN CHEMICAL SOCIETY
pubs.acs.org/JACS
Article

Natural-Language-Interfaced Robotic Synthesis for AI-Copilot-Assisted Exploration of Inorganic Materials

Lin Huang,[▽] Chao Zhang,[▽] Yun Fu,[▽] Yibin Jiang,* Enyu He, Ming-Qiang Qi, Ming-Hao Du, Xiang-Jian Kong, Jun Cheng,* Leroy Cronin,* and Cheng Wang*

Cite This: J. Am. Chem. Soc. 2025, 147, 23014−23025

Read Online

ACCESS | Metrics & More | Article Recommendations | Supporting Information

ABSTRACT: The automation of chemical synthesis presents opportunities to enhance experimental reproducibility and accelerate discovery. Traditional closed-loop approaches, while effective in specific domains, are often constrained by rigid workflows and the requirement for specialized expertise. Here, we introduce a chemical robotic explorer integrated with an artificial intelligence (AI) copilot to enable a more flexible and adaptive synthesis, simplifying the process from inspiration to experimentation. This modular platform uses a large language model (LLM) to map natural language synthetic descriptions to executable unit operations, including temperature control, stirring, liquid and solid handling, filtration, etc. By integrating AI-driven literature searches, real-time experimental design, conversational human−AI interaction, and feedback-based optimization, we demonstrate the capabilities of AI in successfully synthesizing 13 compounds across four distinct classes of inorganic materials: coordination complexes, metal−organic frameworks, nanoparticles, and polyoxometalates. Notably, this approach enabled the discovery of a previously unreported family of Mn−W polyoxometalate clusters, showing the potential of AI-enhanced robotics as a generalizable and adaptable platform for material innovation.

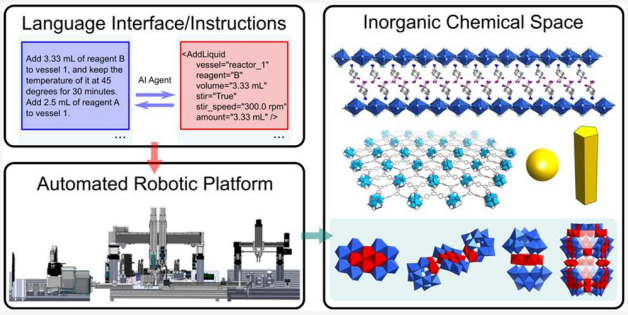

1. INTRODUCTION

Advancements in chemical synthesis are dependent on precise and repeatable experimental operations. However, traditional manual approaches introduce variability and inefficiency, limiting reproducibility and slowing the pace of discovery. Automation offers an increasing opportunity to enhance both the reproducibility and efficiency. Recent advances in artificial intelligence, especially in-line decision-making approaches,[1−5] have introduced a closed-loop methodology for the efficient exploration of chemical spaces, discovering new photocatalysts,[6−9] electrocatalysts,[10] optical nanomaterials,[11−13] chemical reactivity,[14,15] and others.[16−20] While effective in optimizing known reaction spaces, these systems remain constrained by rigid, task-specific workflows that limit their adaptability across diverse synthetic procedures,[21] narrowing the potential for innovation.

To address these challenges, modular and reconfigurable robotic systems have been explored as a promising approach.[6,16,22−24] While some robotic platforms have demonstrated flexibility across diverse procedures,[22−24] proprietary hardware and programming expertise are still required for most of the systems. A cost-effective and scalable solution is needed to shift the focus of researchers from low-level automation control to high-level inspiration, scientific understanding, and decision-making.

One straightforward strategy is to use natural language interfaces to control robotic systems. Early implementations, such as Chemputers and the chemical description language (XDL),[25,26] provided a foundation for translating experimental descriptions into machine-executable instructions. However, traditional natural language processing (NLP) techniques struggled with semantic accuracy,[27] limiting their effectiveness in generating reliable experimental protocols. Recent advances in large language models (LLMs)[28−32] overcome this limitation, demonstrating highly accurate natural-language-to-code translation across systems such as Opentrons,[33] cloud laboratories,[34] Chemputers,[35] and humanoid robots.[36] Unlike template-based NLP approaches, LLMs can generalize across diverse synthetic environments, translating natural language into operating application programming interfaces (APIs), and are well-suited for dynamic and adaptable chemical automation on various hardware.

Received: April 8, 2025
Revised: May 29, 2025
Accepted: May 30, 2025
Published: June 17, 2025

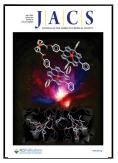

https://doi.org/10.1021/jacs.5c05916
J. Am. Chem. Soc. 2025, 147, 23014−23025

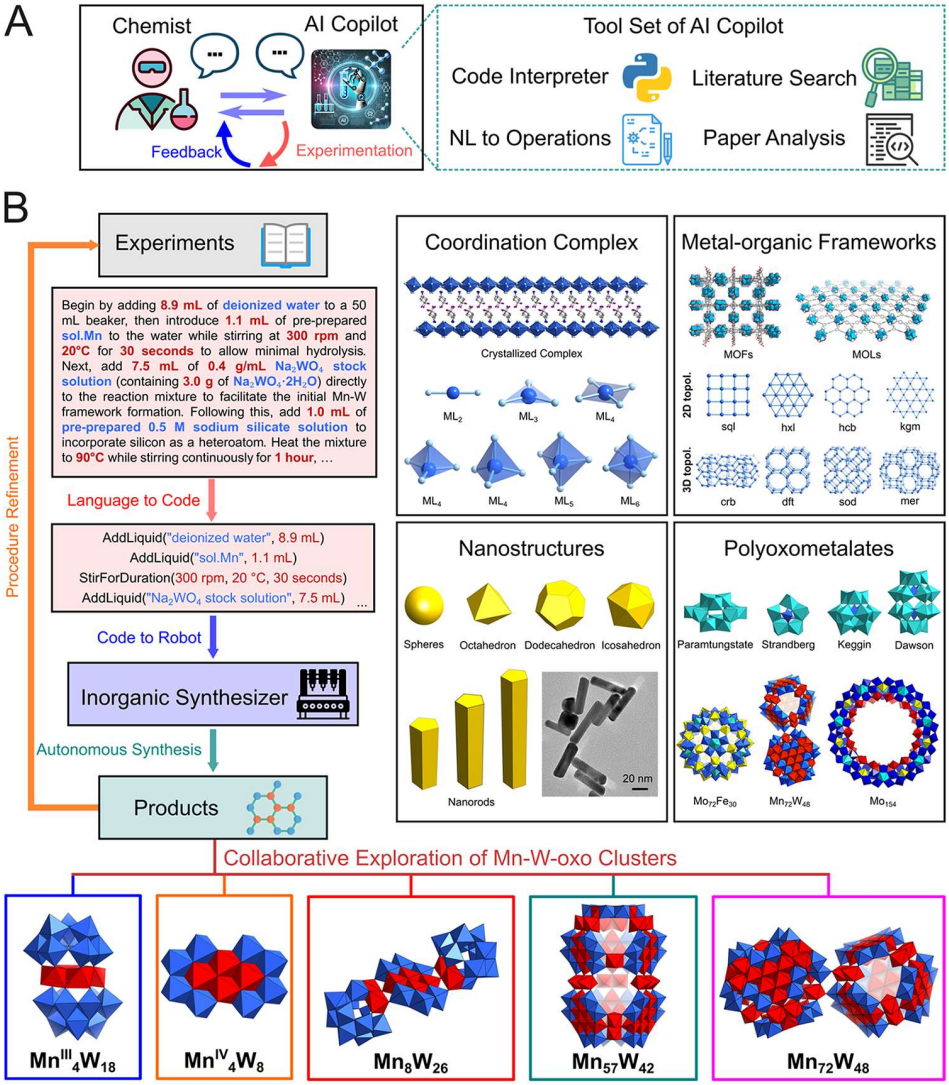

Figure 1. Schematic representation of the exploration of the chemical space with the assistance of AI copilot with flexible and automated synthesis from natural language to products enhanced by LLMs. (A) Exploring the chemical space through a human−AI copilot interaction mode. In this mode, hypotheses are generated through the interactions between human experts and the AI copilot. Several tools, including writing and running normal Python codes, converting language to robotic-executable codes, searching literature from the knowledge base, and analyzing papers, were offered to the AI copilot. Proposed experimental procedures were described in natural language, translated into robotic operations, and executed on the robotic platform. Experimental validation and feedback were used to refine and expand the exploration. (B) Translating experimental procedures from natural language into robotic-executable codes, enabling automated synthesis on the robotic platform, and further refinement of the procedures. This strategy was demonstrated from two aspects: (1) the synthesis of four categories of inorganic materials, including coordination complexes, metal−organic frameworks, nanoparticles, and polyoxometalates. (2) The exploration of Mn−W-oxo clusters based on the previous literature report of $Mn_{72}W_{48}$. The original synthesis procedure was extracted, discussed, and modified to form several exploration templates with changeable experimental parameters. New crystals of Mn_4W_{18}, Mn_4W_8, Mn_8W_{26}, $Mn_{57}W_{42}$, and a new morphology of $Mn_{72}W_{48}$ were discovered in the exploration. Red octahedra: Mn-oxo core. Blue octahedra: W-oxo core.

The natural language interface also facilitates the seamless incorporation of LLMs in the experimental design and optimization. Traditional machine learning methods, in particular, Bayesian optimization[37] and heuristic searching algorithms,[38,39] are widely applied in chemical exploration, but these methods only incorporate very limited chemical knowledge in parameterization or Bayesian priors,[40] limiting their flexibility and efficiency. In contrast, artificial intelligence (AI) agents, which are LLMs equipped with advanced tool-calling capabilities, utilize domain knowledge to enhance decision-making in various fields, including computer science,[41] math,[42] chemistry,[34,43] and computer-assisted design (CAD).[44] These agents, commonly termed AI copilots, actively engage in AI−human collaborative research, enabling human interaction at multiple stages for problem-solving. The natural language interface to chemical synthesis hardware extends the capability of AI copilots to tap into the real-world laboratory, allowing decision-making and execution in a robust automated feedback loop. This significantly enhances copilot-guided chemical synthesis beyond relatively simple operations,[27] predefined procedural templates,[36] or the requirement of manual intervention in complex tasks.[45] Such dynamic, real-time adaptation to experimental feedback and human interpretation is particularly valuable for inorganic

https://doi.org/10.1021/jacs.5c05916
J. Am. Chem. Soc. 2025, 147, 23014−23025

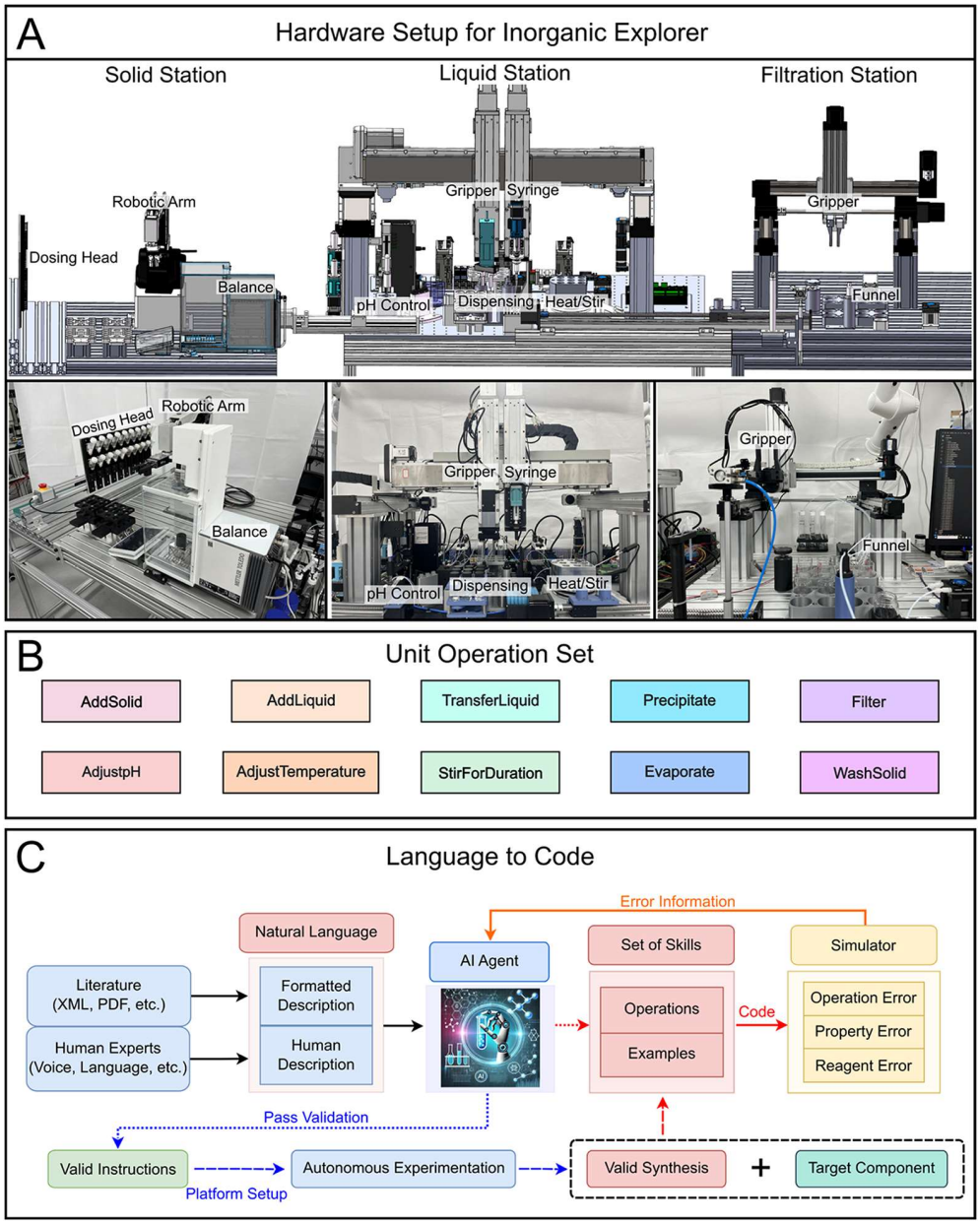

Figure 2. Hardware and software setup of the robotic explorer. (A) The modular design of the robotic explorer comprises three workstations: solid, liquid, and filtration stations. The solid station enables parallel solid dispensing using an automated balance and dispensing heads. The liquid station facilitates liquid handling, pH and temperature control, and capping/uncapping of reactors. The filtration station performs solid/liquid separation using a gripper and funnels. (B) Supported unit operations of the robotic system. The integration of multiple stations enables reagent handling, precise control of reaction conditions, and efficient product separation. These unit operations form the building blocks of the complete synthesis workflow. (C) Workflow for automated synthesis using large language models and the robotic system. Starting from natural language descriptions, the AI agent generates experimental instructions iteratively, incorporating feedback for refinement. Validated instructions are executed on the robotic system to produce the target products.

material synthesis, where synthesis procedures exhibit significant variability and various inspirations are generated and should be tested conveniently.

Herein, we introduce a chemical robotic explorer with a natural language interface to simplify the process from inspiration to experimentation (Figure 1A). The natural language synthesis descriptions are translated into sequential executable unit operations, such as temperature control, stirring, solid and liquid handling, pH adjustment, filtration, and their combinations, allowing for highly flexible experimental workflows. The rigidity of the method was demonstrated by the automated synthesis of coordination complexes,[46,47] metal−organic frameworks (MOFs),[48] nanoparticles (NPs),[49−51] and polyoxometalates (POMs)[52,53] (Figure 1B). Moreover, we utilized the chemical robotic explorer interface with an AI copilot to explore the synthesis of a new family of Mn−W-based polyoxometalates. The AI copilot discusses the experiment plan with human researchers, retrieves literature information for the investigation, controls synthesis hardware through a natural language interface, and refines the exploration strategy iteratively, leading to the discovery of four structurally related new Mn−W-oxo clusters

https://doi.org/10.1021/jacs.5c05916
J. Am. Chem. Soc. 2025, 147, 23014−23025

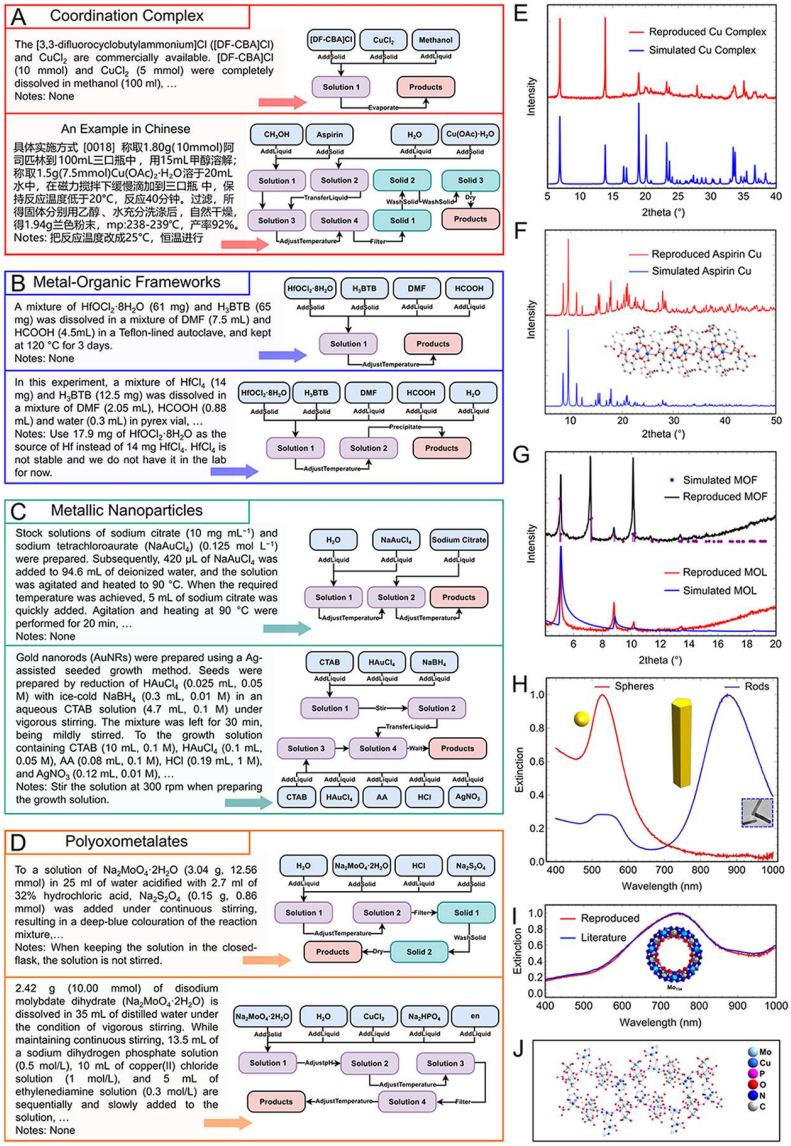

Figure 3. Automated synthesis of inorganic materials using a modular robotic system, from language to products. (A) Synthesis of the coordination complex of $[DF\text{-}CBA]_2CuCl_4$ (top) and aspirin copper (bottom). The procedure for aspirin copper was written in Chinese, which includes mixing the reagents, temperature control, filtration, and washing (see SI Section 2 for translation). (B) Synthesis of Hf-BTB-based metal−organic frameworks (top) and metal−organic monolayers (bottom). For the monolayers, the salt source was replaced through the notes. (C) Synthesis of metallic nanoparticles using the one-pot Turkevich method for Au nanospheres (top) and the seed-mediated method for Au nanorods (bottom). (D) Synthesis of polyoxometalates of Mo_{154} (top) and $(H_2en)[Cu(en)(H_2O)Cu(en)(H_2O)_3][P_2Mo_5O_{23}]$ (bottom). (E) Powder X-ray diffraction (PXRD) characterization of $[DF\text{-}CBA]_2CuCl_4$, confirming the reproduced crystal structure. (F) PXRD patterns of the as-synthesized aspirin copper and simulation from its crystal structure. (G) PXRD patterns for metal−organic frameworks (top) and metal−organic monolayers (bottom), showing agreement between synthesized products and simulations. (H) UV−vis spectra of Au nanospheres from the Turkevich method (red) and nanorods from the seed-mediated synthesis (blue), with additional TEM characterization for nanorods. (I) Normalized UV−vis spectrum of as-synthesized Mo_{154} dissolved in 1 M HCl aqueous solution (red) compared to the literature report (blue). (J) Crystal structure of $(H_2en)[Cu(en)(H_2O)Cu(en)(H_2O)_3][P_2Mo_5O_{23}]$ from the literature report, with single-crystal X-ray diffraction (SXRD) characterization confirming that the lattice constants of the synthesized blue crystals are consistent with it. Note that the full contents of the syntheses are available in SI Section 2.

(namely, Mn_4W_{18}, Mn_4W_8, Mn_8W_{26}, and $Mn_{57}W_{42}$) and an unreported morphology of $Mn_{72}W_{48}$ (Figure 1B). These results highlight the system's capability to accelerate discovery through a seamless integration of AI-driven automation, iterative experimentation, and human−AI collaboration.

2. RESULTS AND DISCUSSION

2.1. Modular Robotic Explorer Augmented by Large Language Models. The hardware of the chemical robotic explorer comprises three workstations: a solid station, a liquid station, and a filtration station. The solid station employs an automated balance for accurate powder dispensing into the reactors. A four-axis robotic arm equipped with a gripper loads and changes dispensing heads and weighing bottles, stream-

https://doi.org/10.1021/jacs.5c05916
J. Am. Chem. Soc. 2025, 147, 23014−23025

lining solid handling tasks. The liquid station features an XYZ moving module with two Z axes: one connected to a rotary gripper for vial handling, capping, and uncapping and the other to a syringe for precise liquid transfer using pipet tips. This station is further enhanced with a pH control module, incorporating inline feedback and base and acid addition. Temperature and stirring control are achieved through an integrated heating mantle. The filtration station is similarly based on an XYZ moving module with a rotary gripper. This gripper loads filtration funnels, grasps reactors for solid dispersion, and pours mixtures for filtration. After filtration, the gripper retrieves a liquid dispensing unit to add solvent to wash the solids in the funnel, if necessary. The filtered liquid is then collected into bottles for further processing. Seamless movement of materials between workstations is facilitated by the robotic arm and XYZ modules with grippers, interconnected via a traveling rail. This integrated system efficiently performs tasks such as solid and liquid addition, liquid transfer, precipitation, filtration, pH adjustment, and temperature control, providing flexible and reliable automation of chemical workflows (Figure 2A,B).

The chemical robotic explorer is enhanced by large language models (GPT-4o and GPT-4),[28,30] which map natural language synthesis procedures into predefined, formatted operations. The LLM-based agentic workflow (Figure 2C) first interprets the synthetic descriptions into a series of predefined executable unit operations and then checks if the required operations are compatible with the current workstation hardware in use. Subsequently, the agent generates the corresponding operation codes, specifying the hardware (e.g., bottles, reagents, and dispensing heads), reagents (including information, such as concentrations and volumes), and reaction conditions. The generated codes then undergo syntax validation against the control systems of the robotic explorer. During this process, units of physical quantities are recognized, standardized, and validated. Any errors detected during the validation are iteratively corrected by the LLM, achieving a syntax validation success rate of ∼97% within three iterations in a benchmark data set of 66 examples for inorganic synthesis. Considering full semantic fidelity to the original synthesis description, the overall success rate was ∼86% (SI Section 2). Once validated, the system performs additional safety and operational checks before execution. Any ambiguities in the generated code are automatically identified and then clarified through conversational interactions before experiment execution. The system also compares required reagents and bottles with the current robotic configuration, automatically identifying missing reagents and, if possible, preparing them by dissolution or dilution. Reactions are scaled according to the reactor volume to prevent overflow. After successful synthesis, experimental descriptions and codes are stored for future reference. The generated codes were integrated into the XDL[25,26] framework, improving interoperability, standardization of experiments, and data exchange. The predefined operations using the APIs from the platform covered 80% of the procedures in the inorganic synthesis data set,[54] capturing a significant portion of the linguistic meaning inherent in chemical synthesis descriptions while not supporting certain operations such as irradiate, burn, grind, etc. (SI Section 2).

2.2. Automated Synthesis from Language Description to Products. The robotic explorer was evaluated for its general applicability in inorganic synthesis through tests across four major categories, including coordination complexes, MOFs, NPs, and POMs (Figure 3).

2.2.1. Coordination Complexes. Coordination complexes represent a fundamental category of inorganic materials. The robotic explorer demonstrated precise reagent handling and solid/liquid manipulation in the synthesis (Figure 3A). One example is the lead-free 2D hybrid organic−inorganic perovskite $[3,3\text{-difluorocyclobutylammonium}]_2CuCl_4$,[55] a multiaxial ferroelectric, which was synthesized via automated solution preparation followed by controlled evaporation to yield crystals. Powder X-ray diffraction (PXRD) characterization confirmed structural consistency with the literature report (Figure 3E). To assess the system's language flexibility, aspirin copper was synthesized from a procedure described in Chinese.[56] This synthesis involved a multistep process, including mixing, crystallization, filtration, and washing. The resulting PXRD patterns were consistent with both the literature report[56] (SI Section 3) and simulations based on its crystal structure[57] (Figure 3F).

2.2.2. Metal−Organic Frameworks (MOFs) and Metal−Organic Layers (MOLs). MOFs and their two-dimensional analogs, MOLs, are another widely studied category of materials for their structural tunability and functionality. Their synthesis, typically performed via one-pot hydrothermal/solvothermal methods, was seamlessly executed by the robotic platform thanks to the precise liquid/solid handling and temperature control (Figure 3B). As a demonstration, Hf-based MOF and MOL materials were synthesized using 1,3,5-tris(4-carboxyphenyl)benzene (H_3BTB) as the ligand.[58] The system showed the capability of modifying synthesis descriptions and tests. The original procedure used $HfCl_4$ as a metal source, but only $HfOCl_2{\cdot}8H_2O$ was available on the platform. The LLM correctly recognized this discrepancy and adapted the generated protocol by substituting $HfCl_4$ with $HfOCl_2{\cdot}8H_2O$ in the desired amount. PXRD analysis confirmed that the synthesized MOFs and MOLs matched the literature structures (Figure 3G).

2.2.3. Nanoparticles (NPs). Nanoparticles constitute another important category of inorganic materials with extensive applications. Their synthesis often requires precise reaction control, particularly in recipe composition and temperature regulation. The system successfully implemented two well-established Au nanoparticle syntheses: the one-pot Turkevich method[59−61] for gold nanospheres and the multistep seed-mediated synthesis[62−64] for gold nanorods (Figure 3C,H). In the Turkevich method, sodium citrate reduced Au^{3+} salts, a reaction requiring controlled heating and precise reagent addition at high temperatures, which can be easily handled by the automation platform via liquid transfer after uncapping a heated reactor. The resulting red solution exhibited an ultraviolet−visible (UV−vis) absorption peak at around 530 nm, which was characteristic of isotropic Au nanoparticles.

For gold nanorods, the system followed a multistep seed-mediated process. First, a seed solution containing ∼2 nm nanoparticles was prepared via the rapid reduction of Au^{3+} salts with $NaBH_4$. This was followed by the preparation of a separate growth solution, to which the addition of the seed solution triggered the nanorod growth. Adjustments in the recipe composition altered the aspect ratio of the nanorods, reflected by shifts in the longitudinal UV−vis absorption peaks. The synthesized Au nanorods showed a peak at 874 nm, close to the reported peak at 857 nm,[64] demonstrating successful replication. Transmission electron microscopy (TEM) further

https://doi.org/10.1021/jacs.5c05916
J. Am. Chem. Soc. 2025, 147, 23014−23025

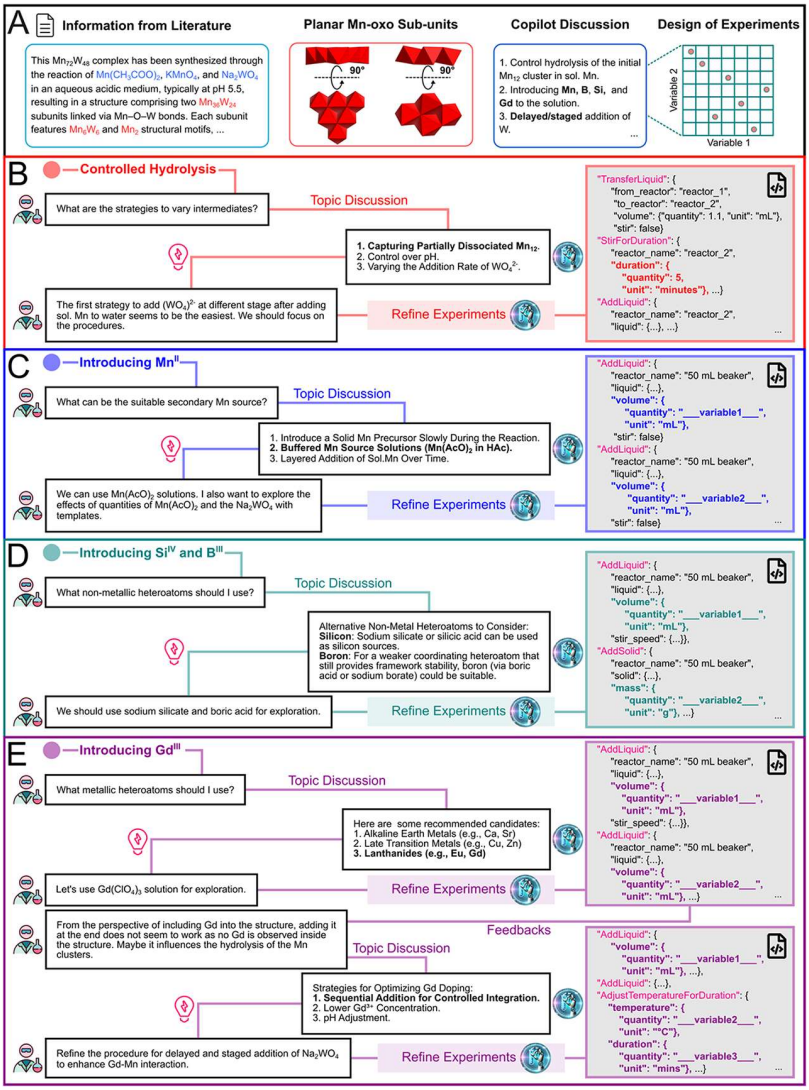

Figure 4. Exploration of the chemical space of Mn–W-oxo clusters with AI copilot. (A) The exploration was guided by human–AI interactions, with literature information summarized and conditions proposed to sample the chemical space by the AI copilot. (B) The copilot-proposed strategies to vary the intermediates controlling the hydrolysis time of sol. Mn were utilized. The sol. Mn was mixed with water and stirred for 2, 5, 15, and 30 min for hydrolysis. This variable is labeled in red in the code block. (C) The copilot offered many ways to introduce additional Mn, and adding $Mn(OAc)_2$ solution was selected. A code template was generated, with variables representing the volumes of Na_2WO_4 and $Mn(OAc)_2$ represented by "___variable1___" and "___variable2___". These variables (labeled blue in the code block) were replaced by actual values through LHS to explore their influences. (D) Inspiration for introducing nonmetallic heteroatoms to influence crystallization. Initially, P, Si, B, and S were recommended, but Si and B with their corresponding reagents were proposed and explored by the copilot. LHS was used to change the quantities of heteroatoms and Na_2WO_4. (E) Inspiration for utilizing metallic heteroatoms to influence crystallization. $Gd(ClO_4)_3$ was introduced to the system, but exploration with LHS to vary quantities of $Gd(ClO_4)_3$ and Na_2WO_4 did not yield new crystals. Thus, procedures were modified for the delayed and staged addition of Na_2WO_4 to enhance the interaction between Mn and Gd. Note that only bullet points from the AI copilots are shown in this figure. The raw context for the interaction is available in SI Section 4.

validated their morphology and size distribution (SI Section 3).

2.2.4. Polyoxometalates (POMs). POMs represent a diverse class of molecular metal-oxo clusters with tunable properties (Figure 3D). $\{Na_{15}[Mo_{126}^{VI}Mo_{28}^{V}O_{462}H_{14}(H_2O)_{70}]_{0.5}[Mo_{124}^{VI}Mo_{28}^{V}O_{457}H_{14}(H_2O)_{68}]_{0.5}\}(Mo_{154})$,[65] a species that displayed the characteristic absorption band of molybdenum blue,[66] was synthesized with a peak at 750 nm that matched the literature report (Figure 3I). While POMs can be readily prepared via liquid/solid handling and temperature/stirring control, there are more complex examples requiring precise pH control, product purification, and separation. pH is a critical parameter in the synthesis of clusters due to its role in fine-tuning the formation of small fragments and their assembly. The robotic system can dynamically adjust the pH to optimize cluster formation and utilize filtration to isolate precipitates, facilitating controlled crystallization from the mother liquor. This was demonstrated in the synthesis of $(H_2en)[Cu(en)(H_2O)Cu(en)(H_2O)_3][P_2Mo_5O_{23}]$ (en = ethylenediamine).[67] The procedure involved in-line pH control, hot filtration, and subsequent crystallization. The resulting blue crystals were analyzed via single-crystal X-ray diffraction (SXRD), confirming their structural consistency with reported lattice parameters (Figure 3J).

https://doi.org/10.1021/jacs.5c05916
J. Am. Chem. Soc. 2025, 147, 23014–23025

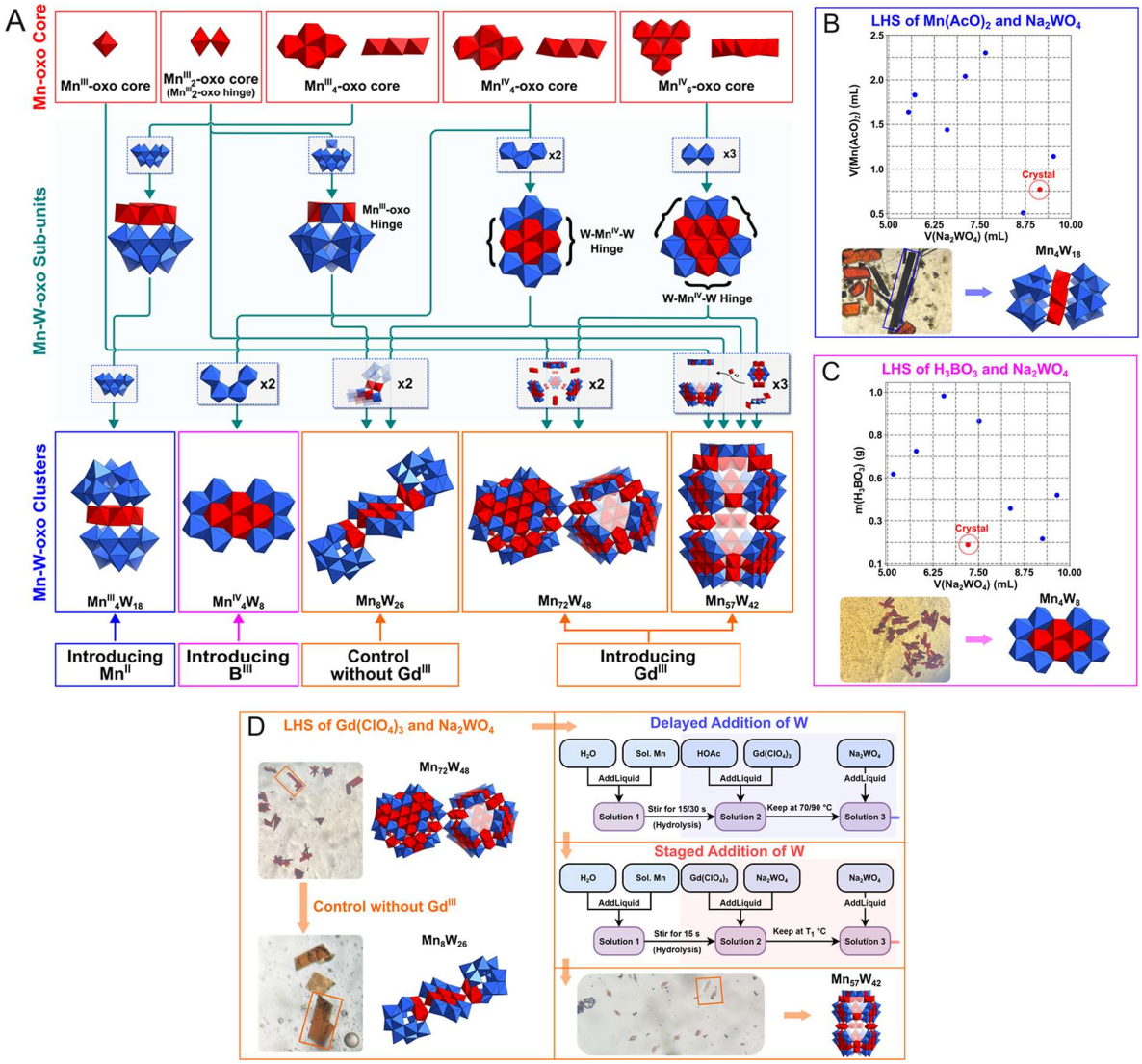

Figure 5. Discovery of structurally related Mn−W-oxo clusters in the exploration. (A) Three clusters, namely, Mn_4W_{18}, Mn_4W_8, Mn_8W_{26}, $Mn_{57}W_{42}$, and a new morphology of $Mn_{72}W_{48}$ were discovered, all showing planar Mn-oxo subunits. (B) The exploration began by introducing $Mn(AcO)_2$ as the secondary Mn source. Black needle-shaped crystals of Mn_4W_{18} were discovered after LHS. The orange crystals were characterized as $Na_8[Mn^{IV}W_6O_{24}]\cdot xH_2O$ (MnW_6). (C) The exploration involves introducing H_3BO_3 to tune the hydrolysis intermediates and possibly heteroatom doping. Red-orange rod-shaped crystals of Mn_4W_8 were discovered after LHS. (D) The exploration by introducing $Gd(ClO_4)_3$, where a new morphology of $Mn_{72}W_{48}$ was observed, and the control experiment without $Gd(ClO_4)_3$ showed orange flask-shaped crystals of Mn_8W_{26} (left bottom). Several variants of the experimental procedures were tried to enhance the role of Gd^{3+}, leading to strong precipitates (right top). Partition of the addition of WO_4^{2-} successfully avoided precipitation (right middle), leading to the synthesis of small orange crystals identified as $Mn_{57}W_{42}$. Red octahedra: Mn-oxo core. Blue octahedra: W-oxo core.

2.3. Inspiration to Experimentation: Collaborative Exploration of Mn−W-Based Polyoxometalates with AI Copilot. The integration of the robotic platform with natural language processing capabilities enabled highly flexible and adaptive experimentation. To fully harness its potential, hardware control functions are delegated to an AI copilot, unifying idea generation with a streamlined transition from inspiration to experimentation. The AI copilot was equipped with the relevant literature and capable of code interpretation, paper analysis, and retrieval-augmented generation (RAG) using OpenAI's GPT store feature. When new ideas emerge, the copilot seamlessly translates natural language inputs into robot-executable code, integrating them into adaptive workflows for automated execution.

This system was applied to explore the synthesis of Mn−W-based polyoxometalate (Mn−W-oxo) clusters. In a previously reported $Mn_{72}W_{48}$ cluster,[68,69] two connected tetrahedral cages were observed, each formed by four planar $Mn_6^{IV}W_6$-oxo as faces linked at the edges by Mn_2^{III}-oxo clusters. The distinctive planar multi-Mn^{IV}-oxo plate[70−74] serves as an effective building block for constructing robust cages. Thus, the goal was set to thoroughly explore the structural diversity of Mn−W-oxo clusters in the chemical space and identify missing crystalline structures with the assistance of the copilot.

We started from the synthetic condition of $Mn_{72}W_{48}$, which began with the preparation of a mixture of $Mn(AcO)_2$, $KMnO_4$, and 60% v/v acetic acid[75] (referred to as sol. Mn), a solution that can crystallize the well-known $Mn_{12}O_{12}(O_2CMe)_{16}(H_2O)_4$ cluster with a $Mn_4^{IV}O_4$ cubic

https://doi.org/10.1021/jacs.5c05916
J. Am. Chem. Soc. 2025, 147, 23014−23025

core. The sol. Mn was then mixed with Na_2WO_4 and heated at 90 °C before being filtered to crystallize $Mn_{72}W_{48}$. Rich Mn^{IV}-oxo subunits may exist in the solution to be captured by W-based species. Very little knowledge, except two literature reports,[68,69] is available to guide the search. Trials, serendipitous findings, and systematic refinements were recorded throughout the exploration. Inspirations drawn from brainstorming with the AI copilot were automatically converted to experimental implementations, iteratively refining the synthesis in 65 rounds of human−AI interactions, and eventually led to the discovery of a series of Mn−W-oxo clusters (Figures 4 and5A).

2.3.1. Controlled Hydrolysis. To go beyond the $Mn_{72}W_{48}$ cluster, a logical strategy is to change the condition for sol. Mn hydrolysis tunes the distribution of different Mn-oxo fragments or different species are added to capture the decomposed intermediates, as proposed by the copilot. After 14 rounds of iterative interactions (Figure 4B), the human researcher and the copilot decided to focus on a hydrolyzing sol. Mn by diluting it into a large amount of water (∼9-fold) for a precisely controlled period (2−30 min), before the addition of Na_2WO_4 for varied intermediate capturing. The automated synthesis allowed the accurate control of the hydrolysis time as compared to manual operation. However, this endeavor did not lead to much success in producing new crystals. Still, the hydrolysis period was shown to be very critical, as the hydrolysis periods above 2 min lead to strong precipitation of the Mn species, decreasing the amount of soluble Mn-oxo fragments that can be captured and utilized by polytungstates for crystal formation later.

2.3.2. Increased Mn in the Growth Solution. Observing the hydrolysis of Mn species to generate amorphous solids that were removed in the synthesis, the copilot and the human researcher realized that the low concentration of the remaining Mn in solution may be limiting for cluster formation. To address this issue, setting a higher concentration of Mn species for the reaction solution was discussed and explored within 7 rounds of discussions (Figure 4C). As the sol. Mn contains 60% v/v of HOAc, adding $Mn(OAc)_2$ as the secondary Mn source was suggested by the copilot, increasing Mn concentration without interrupting the pH of the reaction at the same time. For more efficient exploration, the AI copilot created a procedural template to use Latin hypercube sampling (LHS)[76] for the systematic screening of experimental conditions, including the quantities of $Mn(OAc)_2$ and Na_2WO_4. The quick generation of executable code from inspirations streamlined the exploration process. A black needle-shaped crystal was obtained in the LHS. Single-crystal X-ray diffraction (SXRD) analysis revealed a new structure with the formula of $Na_8H_4[Mn_4^{III}O_2(OH)_2(H_3W_9O_{33})_2]\cdot xH_2O$ (Mn_4W_{18}) (Figure 5B), a planar Mn_4^{III}-oxo core sandwiched between two $[W_9O_{33}]$ fragments. Mn^{III} instead of Mn^{IV} units were obtained, possibly due to the additional Mn^{II} in $Mn(OAc)_2$ reacting with Mn^{IV} in sol. Mn to form Mn^{III}. Additionally, orange bulk crystals coformed under the same conditions as byproducts, which were identified as the previously reported $Na_8[Mn^{IV}W_6O_{24}]\cdot xH_2O$ (MnW_6).[77]

2.3.3. Nonmetallic Modulator: Silicon (Na_2SiO_3) and Boron (H_3BO_3). Besides adding more Mn, stabilizing the Mn intermediates to prevent early precipitation may also retain a higher Mn concentration for the synthesis. To further diversify the Mn−W framework, the copilot suggested including reagents containing heteroatoms or modulators in the growth solution to add variation and capture new species. For nonmetallic reagents, species of phosphorus (P), silicon (Si), boron (B), and sulfur (S) were all proposed. However, to avoid forming insoluble manganese compounds, the exploration was refined to focus on Si and B after a short query of existing knowledge of the copilot, with experiments executed within 14 rounds of interactions (see Figure 4D and SI Section 4).

For Si, sodium silicate (Na_2SiO_3) was introduced. However, high solution viscosity was observed, complicating filtration, possibly due to the formation of polymeric Mn−W−Si species. Switching to B with boric acid (H_3BO_3), the copilot highlighted the controlled solubility, gentle coordination tendency, and mild acidity of H_3BO_3. An LHS exploration of the experimental space led to the formation of red-orange rod-shaped crystals (Figure 5C). SXRD analysis revealed their structure as $Na_8H_4[Mn_4^{IV}O_2(W_4O_{18})_2]\cdot yH_2O$ (Mn_4W_8), containing a parallelogram Mn_4^{IV}-oxo core with two sets of $[W_4O_{18}]$ units attached to its acute edges to form a planar $Mn_4^{IV}W_8$-oxo cluster. The structure does not contain boron but did not form without the addition of H_3BO_3 addition. B-related species may serve as a pH buffer or participate in the early coordination of species but be replaced later by the W-species. This addition of modulators in intermediate steps broadens the possible exploration space of Mn−W clusters.

2.3.4. Metallic Modulator: Gadolinium ($Gd(ClO_4)_3$). As suggested earlier by the copilot, the addition of different metals can diversify the structure, proposing the idea of adding species from alkaline earth metals (Ca, Sr), late transition metals (Cu, Zn), and lanthanides (Eu, Gd) to main group metals (Al) in the synthesis. However, we would like to focus on the Mn as the transition metal and seek information about lanthanides as additives. Within 10 rounds of interactions, the next step was determined to introduce Gd^{3+} as an additive (Figure 4E), as the copilot reasoned that it can potentially introduce magnetic properties and serve as a network stabilizer to bind and terminate Mn intermediates. Similar to B-additives, Gd^{3+} may also affect the intermediate formation but be replaced in the final product, acting as a catalyst. $Gd(ClO_4)_3$ was used in the investigation due to its high solubility. LHS-guided experiments yielded two samples, producing $Mn_{72}W_{48}$ with a deep-reddish flask shape, which represents a different morphology compared to the previously reported black crystals (Figure 5D, left top, and SI Section 4). Interestingly, a control experiment without adding the $Gd(ClO_4)_3$ solution but adding water serendipitously produced bright orange flask-shaped crystals, which were later identified as $Na_{24}[Mn_4^{IV}O_4(W_3O_{14})_2(H_2Mn_2^{III}W_{10}O_{37})_2]\cdot zH_2O$ (Mn_8W_{26}) through SXRD (Figure 5D, left bottom), containing a planar $Mn_4^{IV}W_6$-oxo unit. The ease of translating incentives into experimental actions encourages researchers to explore a wider range of possibilities, thereby increasing the likelihood of discovering unexpected results.

In the absence of an observable impact of Gd^{3+} in the Mn−W-oxo cluster formation, the copilot suggested adjusting the experimental conditions to ensure a longer reaction time for incorporating Gd (Figure 4E). With further interactions, a plan of the sol. Mn prehydrolysis with Gd is proposed by the copilot and refined later. In this procedure (Figure 5D, right top), Gd and sol. Mn were mixed, heated, and then WO_4^{2-} was introduced, but severe Mn precipitation occurred during the heating due to the lack of a stabilizer like WO_4^{2-}. Follow-up ideas, such as reducing hydrolysis time and adding acetic acid to stabilize the solution, also led to strong precipitation.

https://doi.org/10.1021/jacs.5c05916
J. Am. Chem. Soc. 2025, 147, 23014−23025

Eventually, a revised procedure (Figure 5D, right middle) was proposed by the copilot. It split WO_4^{2-} into two portions and was refined to be as follows: (1) Mn, Gd, and part of WO_4^{2-} were mixed and heated and then (2) the remaining WO_4^{2-} was added, and the mixture was heated again. This strategy mitigated severe precipitation issues, demonstrating the copilot's capability to refine experimental protocols through 18 rounds of interactions overall. As shown in Figure 5D at the bottom right, small orange crystals were produced from the trials. SXRD revealed its structure as $Na_9H_{23}\{[Mn^{II}(H_2O)_2]_3[Mn_2^{III}(H_2O)_4]_9[(Mn_6^{IV}O_7)_4(Mn_4^{IV}O_4)_3][W_2O_{10}]_{12}[W_3O_{14}]_6\}\cdot wH_2O$ ($Mn_{57}W_{42}$), containing planar $Mn_4^{IV}W_6$-oxo and $Mn_6^{IV}W_6$-oxo subunits, both featuring W−Mn^{IV}−W hinges that were interconnected via Mn_2^{III}-oxo subunits. The overall structure is a large cage composed of seven $Mn_4^{IV}W_6$ faces or $Mn_6^{IV}W_6$ faces.

Through the exploration of various synthesis protocols, the structural landscape of Mn−W-oxo clusters has been studied (Figure 5A). A series of Mn-oxo subunits are identified as the building blocks for the clusters. In particular, the Mn_4^{IV}-oxo and Mn_6^{IV}-oxo subunits tend to coordinate with W-oxo subunits to form planar structures. $Mn^{III}{}_2$-oxo subunits often serve as connectors, linking to these planar units through W−Mn^{IV}−W hinges and residing on a separate plane. These behaviors are commonly observed in clusters, such as $Mn_4^{IV}W_8$, Mn_8W_{26}, $Mn_{72}W_{48}$, and $Mn_{57}W_{42}$. In contrast, Mn^{III}-oxo subunits are observed to bind to vacant metatungstates to form substituted polyanions. One example is $Mn_4^{III}W_{18}$, where the planar Mn_4^{III}-oxo subunit captures two trivacant metatungstates to form a stable cluster. The tendency of Mn^{III}-oxo subunits linking to metatungstates is also observed in Mn_8W_{26}, where the Mn_2^{III}-oxo subunit not only connects to a W−Mn^{IV}−W hinge of a Mn_4W_6 subunit but also binds to a bivacant metatungstate. These insights into subunit behavior and assembly patterns were enabled by AI copilot, which played a critical role in exploring the chemical space for cluster formation.

3. CONCLUSIONS

In conclusion, the integration of AI-driven robotic systems and natural language processing presents a transformative opportunity in chemical synthesis. By combining modular robotic platforms with advanced large language models and AI copilots, this approach not only enhances the flexibility and efficiency of experimental workflows but also opens new avenues for the exploration of complex chemical systems. The successful synthesis of diverse inorganic materials, such as coordination complexes, MOFs, NPs, and POMs, underscores the potential of this technology to streamline the synthesis and expand chemical discovery. Moreover, the dynamic collaboration between AI and human chemists, facilitated by the AI copilot, enables more comprehensive and adaptive experimental design and simplifies the inspiration-to-experimentation process, expanding the scope of traditional closed-loop optimization. As demonstrated in the exploration of Mn−W-oxo clusters, this system offers the ability to navigate large chemical spaces, refine experimental conditions in real time, and discover new materials with greater efficiency by avoiding being trapped in a fixed procedure. Moving forward, the continued advancement of AI-powered chemical exploration tools holds promise for accelerating the pace of material discovery and unlocking new frontiers in chemical research.

4. MATERIALS AND METHODS

4.1. Robotic Platform. The robotic platform, comprising multiple in-house-constructed workstations and modules, was designed for automated synthesis and experimentation. Details of its architecture and operation are provided in SI Section 1. The source code for controlling the platform is available on GitHub. The hardware design used in this work is available on figshare.

4.2. Agentic Workflow from Language to Code. The workflow, including translation processes and benchmark evaluations, is described in SI Section 2.

4.3. Chemical Reagents. All aqueous solutions were prepared by using type I water. A complete list of reagents used for synthesizing the reproduced compounds from the literature and for exploring Mn−W-oxo clusters can be found in SI Sections 3 and 4, respectively.

4.4. From Natural Language to Products. The full details of executing codes from natural language to synthesizing the target compounds with their corresponding characterization and data analysis are available in SI Section 3.

4.5. AI-Assisted Exploration. The AI copilot was developed using features from the GPT store with an external API to convert natural language into executable code. The exploration process was guided by the AI copilot and the human expert, which involved refining experimental conditions based on the iterative feedback. The full discussion of experimental planning and optimization is provided in SI Section 4 and GitHub. The details of the structural characterization of $Mn_4^{IV}W_8$ (CCDC 2434279), Mn_4W_{18} (CCDC 2434280), Mn_8W_{26} (CCDC 2434281), and $Mn_{57}W_{42}$ (CCDC 2440048) are also available in SI Section 4.

■ ASSOCIATED CONTENT

Data Availability Statement

All of the material characterization data are available on figshare through 10.6084/m9.figshare.29335532. Other data are available on GitHub https://github.com/Wang-Group/ChemicalExplorerCopilot/. All of the relevant codes are available on GitHub https://github.com/Wang-Group/ChemicalExplorerCopilot/. All the hardware design used in this work is available on figshare through 10.6084/m9.figshare.29335310.

Supporting Information

The Supporting Information is available free of charge at https://pubs.acs.org/doi/10.1021/jacs.5c05916.

Additional experimental details, materials, and methods, including photographs of the experimental setup (PDF)

The record of an exploration experiment to control the hydrolysis of sol. Mn (Movie S1) (MP4)

Demonstration of adding solids on the robotic platform (Movie S2) (MP4)

Demonstration of adding and transferring liquid on the robotic platform (Movie S3) (MP4)

Demonstration of adjusting pH on the robotic platform (Movie S4) (MP4)

Demonstration of adjusting temperature on the robotic platform (Movie S5) (MP4)

Demonstration of filtration and wash solid operations on the robotic platform (Movie S6) (MP4)

Accession Codes

Deposition Numbers 2434279−2434281 and 2440048 contain the supplementary crystallographic data for this paper. These data can be obtained free of charge via the joint Cambridge Crystallographic Data Centre (CCDC) and Fachinformationszentrum Karlsruhe Access Structures service.

https://doi.org/10.1021/jacs.5c05916
J. Am. Chem. Soc. 2025, 147, 23014−23025

AUTHOR INFORMATION

Corresponding Authors

Yibin Jiang − *State Key Laboratory of Physical Chemistry of Solid Surfaces, iChEM, College of Chemistry and Chemical Engineering, Xiamen University, Xiamen 361005, P. R. China; Innovation Laboratory for Sciences and Technologies of Energy Materials of Fujian Province (IKKEM), Xiamen 361005, P. R. China; School of Chemistry, The University of Glasgow, Glasgow G12 8QQ, U.K.;* orcid.org/0000-0002-9766-5679; Email: yibin_jiang@outlook.com

Jun Cheng − *State Key Laboratory of Physical Chemistry of Solid Surfaces, iChEM, College of Chemistry and Chemical Engineering, Xiamen University, Xiamen 361005, P. R. China; Innovation Laboratory for Sciences and Technologies of Energy Materials of Fujian Province (IKKEM), Xiamen 361005, P. R. China; Institute of Artificial Intelligence, Xiamen University, Xiamen 361005, P. R. China;* orcid.org/0000-0001-6971-0797; Email: chengjun@xmu.edu.cn

Leroy Cronin − *School of Chemistry, The University of Glasgow, Glasgow G12 8QQ, U.K.;* orcid.org/0000-0001-8035-5757; Email: Lee.Cronin@Glasgow.ac.uk

Cheng Wang − *State Key Laboratory of Physical Chemistry of Solid Surfaces, iChEM, College of Chemistry and Chemical Engineering, Xiamen University, Xiamen 361005, P. R. China; Innovation Laboratory for Sciences and Technologies of Energy Materials of Fujian Province (IKKEM), Xiamen 361005, P. R. China;* orcid.org/0000-0002-7906-8061; Email: wangchengxmu@xmu.edu.cn

Authors

Lin Huang − *State Key Laboratory of Physical Chemistry of Solid Surfaces, iChEM, College of Chemistry and Chemical Engineering, Xiamen University, Xiamen 361005, P. R. China;* orcid.org/0000-0003-1683-2103

Chao Zhang − *State Key Laboratory of Physical Chemistry of Solid Surfaces, iChEM, College of Chemistry and Chemical Engineering, Xiamen University, Xiamen 361005, P. R. China; Innovation Laboratory for Sciences and Technologies of Energy Materials of Fujian Province (IKKEM), Xiamen 361005, P. R. China; Henan Key Laboratory of Polyoxometalate Chemistry, College of Chemistry and Molecular Sciences, Henan University, Kaifeng, Henan 475004, P. R. China;* orcid.org/0000-0002-7400-5803

Yun Fu − *National Science Library, Chinese Academy of Sciences, Beijing 100190, P. R. China*

Enyu He − *State Key Laboratory of Physical Chemistry of Solid Surfaces, iChEM, College of Chemistry and Chemical Engineering, Xiamen University, Xiamen 361005, P. R. China*

Ming-Qiang Qi − *State Key Laboratory of Physical Chemistry of Solid Surfaces, iChEM, College of Chemistry and Chemical Engineering, Xiamen University, Xiamen 361005, P. R. China*

Ming-Hao Du − *State Key Laboratory of Physical Chemistry of Solid Surfaces, iChEM, College of Chemistry and Chemical Engineering, Xiamen University, Xiamen 361005, P. R. China*

Xiang-Jian Kong − *State Key Laboratory of Physical Chemistry of Solid Surfaces, iChEM, College of Chemistry and Chemical Engineering, Xiamen University, Xiamen 361005, P. R. China;* orcid.org/0000-0003-0676-6923

Complete contact information is available at: https://pubs.acs.org/10.1021/jacs.5c05916

Author Contributions

[▽]L.H., C.Z., and Y.F. contributed equally to this work.

Notes

The authors declare no competing financial interest.

ACKNOWLEDGMENTS

The authors gratefully acknowledge insightful discussions with Boxuan Zhao from Peking University, Dr. Emma Clarke and Dr. J. Sebastián Manzano from Chemify Ltd., and Dr. Dean Thomas, Dr. Daniel Salley, Dr. Graham Keenan, and Dr. Nikita Smirnov from the University of Glasgow. The authors also acknowledge financial support from the National Key R&D Program of China (2021YFA1502500), the National Natural Science Foundation of China (22125502, 22461160282, 22121001, 92461305), the Fundamental Research Funds for the Central Universities (20720240151), the EPSRC (nos. EP/L023652/1; EP/R009902/1; EP/R020914/1; EP/R01308X/1; EP/S017046/1; EP/S019472/1; and EP/V048341/1), and the European Research Council (project 670467 SMART-POM).

REFERENCES

(1) Ureel, Y.; Dobbelaere, M. R.; Ouyang, Y.; De Ras, K.; Sabbe, M. K.; Marin, G. B.; Van Geem, K. M. Active Machine Learning for Chemical Engineers: A Bright Future Lies Ahead! *Engineering* **2023**, *27*, 23−30.

(2) Masson, J.-B. Counting biomolecules with Bayesian inference. *Nat. Comput. Sci.* **2022**, *2* (2), 74−75.

(3) Häse, F.; Aldeghi, M.; Hickman, R. J.; Roch, L. M.; Aspuru-Guzik, A. Gryffin: An algorithm for Bayesian optimization of categorical variables informed by expert knowledge. *Appl. Phys. Rev.* **2021**, *8* (3), No. 031406.

(4) Häse, F.; Roch, L. M.; Kreisbeck, C.; Aspuru-Guzik, A. Phoenics: A Bayesian Optimizer for Chemistry. *ACS Cent. Sci.* **2018**, *4* (9), 1134−1145.

(5) Mouret, J.-B.; Clune, J.Illuminating Search Spaces by Mapping Elites. 2015, arXiv:1504.04909. arXiv.org e-Printarchive. https://arxiv.org/abs/1504.04909. (acccessed April 20, 2015).

(6) Burger, B.; Maffettone, P. M.; Gusev, V. V.; Aitchison, C. M.; Bai, Y.; Wang, X.; Li, X.; Alston, B. M.; Li, B.; Clowes, R.; et al. A mobile robotic chemist. *Nature* **2020**, *583* (7815), 237−241.

(7) Li, X.; Che, Y.; Chen, L.; Liu, T.; Wang, K.; Liu, L.; Yang, H.; Pyzer-Knapp, E. O.; Cooper, A. I. Sequential closed-loop Bayesian optimization as a guide for organic molecular metallophotocatalyst formulation discovery. *Nat. Chem.* **2024**, *16* (8), 1286−1294.

(8) Angello, N. H.; Friday, D. M.; Hwang, C.; Yi, S.; Cheng, A. H.; Torres-Flores, T. C.; Jira, E. R.; Wang, W.; Aspuru-Guzik, A.; Burke, M. D.; et al. Closed-loop transfer enables artificial intelligence to yield chemical knowledge. *Nature* **2024**, *633* (8029), 351−358.

(9) Slattery, A.; Wen, Z.; Tenblad, P.; Sanjosé-Orduna, J.; Pintossi, D.; den Hartog, T.; Noël, T. Automated self-optimization, intensification, and scale-up of photocatalysis in flow. *Science* **2024**, *383* (6681), No. eadj1817.

(10) Zhu, Q.; Huang, Y.; Zhou, D.; Zhao, L.; Guo, L.; Yang, R.; Sun, Z.; Luo, M.; Zhang, F.; Xiao, H.; et al. Automated synthesis of oxygen-producing catalysts from Martian meteorites by a robotic AI chemist. *Nat. Synth.* **2024**, *3* (3), 319−328.

(11) Jiang, Y.; Salley, D.; Sharma, A.; Keenan, G.; Mullin, M.; Cronin, L. An artificial intelligence enabled chemical synthesis robot for exploration and optimization of nanomaterials. *Sci. Adv.* **2022**, *8* (40), No. eabo2626.

(12) Zhao, H.; Chen, W.; Huang, H.; Sun, Z.; Chen, Z.; Wu, L.; Zhang, B.; Lai, F.; Wang, Z.; Adam, M. L.; et al. A robotic platform for

the synthesis of colloidal nanocrystals. *Nat. Synth.* **2023**, *2* (6), 505−514.
(13) Salley, D.; Keenan, G.; Grizou, J.; Sharma, A.; Martín, S.; Cronin, L. A nanomaterials discovery robot for the Darwinian evolution of shape programmable gold nanoparticles. *Nat. Commun.* **2020**, *11* (1), No. 2771.
(14) Caramelli, D.; Granda, J. M.; Mehr, S. H. M.; Cambié, D.; Henson, A. B.; Cronin, L. Discovering New Chemistry with an Autonomous Robotic Platform Driven by a Reactivity-Seeking Neural Network. *ACS Cent. Sci.* **2021**, *7* (11), 1821−1830.
(15) Dai, T.; Vijayakrishnan, S.; Szczypiński, F. T.; Ayme, J.-F.; Simaei, E.; Fellowes, T.; Clowes, R.; Kotopanov, L.; Shields, C. E.; Zhou, Z.; et al. Autonomous mobile robots for exploratory synthetic chemistry. *Nature* **2024**, *635* (8040), 890−897.
(16) Zhu, Q.; Zhang, F.; Huang, Y.; Xiao, H.; Zhao, L.; Zhang, X.; Song, T.; Tang, X.; Li, X.; He, G.; et al. An all-round AI-Chemist with a scientific mind. *Natl. Sci. Rev.* **2022**, *9* (10), No. nwac190.
(17) Su, Y.; Wang, X.; Ye, Y.; Xie, Y.; Xu, Y.; Jiang, Y.; Wang, C. Automation and machine learning augmented by large language models in a catalysis study. *Chem. Sci.* **2024**, *15* (31), 12200−12233.
(18) Tom, G.; Schmid, S. P.; Baird, S. G.; Cao, Y.; Darvish, K.; Hao, H.; Lo, S.; Pablo-García, S.; Rajaonson, E. M.; Skreta, M.; et al. Self-Driving Laboratories for Chemistry and Materials Science. *Chem. Rev.* **2024**, *124* (16), 9633−9732.
(19) MacLeod, B. P.; Parlane, F. G. L.; Morrissey, T. D.; Häse, F.; Roch, L. M.; Dettelbach, K. E.; Moreira, R.; Yunker, L. P. E.; Rooney, M. B.; Deeth, J. R.; et al. Self-driving laboratory for accelerated discovery of thin-film materials. *Sci. Adv.* **2020**, *6* (20), No. eaaz8867.
(20) Szymanski, N. J.; Rendy, B.; Fei, Y.; Kumar, R. E.; He, T.; Milsted, D.; McDermott, M. J.; Gallant, M.; Cubuk, E. D.; Merchant, A.; et al. An autonomous laboratory for the accelerated synthesis of novel materials. *Nature* **2023**, *624* (7990), 86−91.
(21) Salley, D.; Manzano, J. S.; Kitson, P. J.; Cronin, L. Robotic Modules for the Programmable Chemputation of Molecules and Materials. *ACS Cent. Sci.* **2023**, *9* (8), 1525−1537.
(22) Manzano, J. S.; Hou, W.; Zalesskiy, S. S.; Frei, P.; Wang, H.; Kitson, P. J.; Cronin, L. An autonomous portable platform for universal chemical synthesis. *Nat. Chem.* **2022**, *14* (11), 1311−1318.
(23) Coley, C. W.; Thomas Iii, D. A.; Lummiss, J. A. M.; Jaworski, J. N.; Breen, C. P.; Schultz, V.; Hart, T.; Fishman, J. S.; Rogers, L.; Gao, H.; et al. A robotic platform for flow synthesis of organic compounds informed by AI planning. *Science* **2019**, *365* (6453), No. eaax1566.
(24) Steiner, S.; Wolf, J.; Glatzel, S.; Andreou, A.; Granda, J. M.; Keenan, G.; Hinkley, T.; Aragon-Camarasa, G.; Kitson, P. J.; Angelone, D.; Cronin, L. Organic synthesis in a modular robotic system driven by a chemical programming language. *Science* **2019**, *363* (6423), No. eaav2211.
(25) Mehr, S. H. M.; Craven, M.; Leonov, A.; Keenan, G.; Cronin, L. A universal system for digitization and automatic execution of the chemical synthesis literature. *Science* **2020**, *370* (6512), 101−108.
(26) Cronin Group. XDL 2.0 Standard. https://croningroup.gitlab.io/chemputer/xdl/standard/index.html.
(27) Yoshikawa, N.; Skreta, M.; Darvish, K.; Arellano-Rubach, S.; Ji, Z.; Bjørn Kristensen, L.; Li, A. Z.; Zhao, Y.; Xu, H.; Kuramshin, A.; et al. Large language models for chemistry robotics. *Auton. Robots* **2023**, *47* (8), 1057−1086.
(28) Achiam, J.; Adler, S.; Agarwal, S.; Ahmad, L.; Akkaya, I.; Aleman, F. L.; Almeida, D.; Altenschmidt, J.; Altman, S.; Anadkat, S. Gpt-4 Technical Report **2023**, arXiv:2303.08774. arXiv.org e-Printarchive. https://arxiv.org/abs/2303.08774. (acccessed March 15, 2023).
(29) Guo, D.; Yang, D.; Zhang, H.; Song, J.; Zhang, R.; Xu, R.; Zhu, Q.; Ma, S.; Wang, P.DeepSeek-AI; et al.. DeepSeek-R1: Incentivizing Reasoning Capability in LLMs via Reinforcement Learning. 2025, arXiv:2501.12948. arXiv.org e-Printarchive. https://arxiv.org/abs/2501.12948. Acccessed January 22, 2025).
(30) Hurst, A.; Lerer, A.; Goucher, A. P.; Perelman, A.; Ramesh, A.; Clark, A.; Ostrow, A.; Welihinda, A.; Hayes, A.; Radford, A. et al. Gpt-4o System Card **2024**, arXiv:2410.21276. arXiv.org e-Printarchive. https://arxiv.org/abs/2410.21276. (acccessed October 25, 2024).
(31) Fébba, D.; Egbo, K.; Callahan, W. A.; Zakutayev, A. From text to test: AI-generated control software for materials science instruments. *Digital Discovery* **2025**, *4* (1), 35−45.
(32) Liu, Y.; Checa, M.; Vasudevan, R. K. Synergizing human expertise and AI efficiency with language model for microscopy operation and automated experiment design*. *Mach. Learn.: Sci. Technol.* **2024**, *5* (2), No. 02LT01.
(33) Ruan, Y.; Lu, C.; Xu, N.; He, Y.; Chen, Y.; Zhang, J.; Xuan, J.; Pan, J.; Fang, Q.; Gao, H.; et al. An automatic end-to-end chemical synthesis development platform powered by large language models. *Nat. Commun.* **2024**, *15* (1), No. 10160.
(34) Boiko, D. A.; MacKnight, R.; Kline, B.; Gomes, G. Autonomous chemical research with large language models. *Nature* **2023**, *624* (7992), 570−578.
(35) Pagel, S.; Jirasek, M.; Cronin, L. Validation of the Scientific Literature via Chemputation Augmented by Large Language Models. 2024, arXiv:2410.06384. arXiv.org e-Printarchive. https://arxiv.org/abs/2410.06384. (acccessed October 08, 2024).
(36) Song, T.; Luo, M.; Zhang, X.; Chen, L.; Huang, Y.; Cao, J.; Zhu, Q.; Liu, D.; Zhang, B.; Zou, G.; et al. A Multiagent-Driven Robotic AI Chemist Enabling Autonomous Chemical Research On Demand. *J. Am. Chem. Soc.* **2025**, *147* (15), 12534−12545.
(37) Shields, B. J.; Stevens, J.; Li, J.; Parasram, M.; Damani, F.; Alvarado, J. I. M.; Janey, J. M.; Adams, R. P.; Doyle, A. G. Bayesian reaction optimization as a tool for chemical synthesis. *Nature* **2021**, *590* (7844), 89−96.
(38) Vikhar, P. A. In *Evolutionary Algorithms: A Critical Review and Its Future Prospects*, International Conference on Global Trends in Signal Processing, Information Computing and Communication (ICGTSPICC), 22−24 Dec. 2016; IEEE, 2016; pp 261−265.
(39) Pugh, J. K.; Soros, L. B.; Stanley, K. O. Quality Diversity: A New Frontier for Evolutionary Computation. *Front. Robot. AI* **2016**, *3*, No. 40.
(40) Mehr, S. H. M.; Caramelli, D.; Cronin, L. Digitizing chemical discovery with a Bayesian explorer for interpreting reactivity data. *Proc. Natl. Acad. Sci. U.S.A.* **2023**, *120* (17), No. e2220045120.
(41) Lu, C.; Lu, C.; Lange, R. T.; Foerster, J.; Clune, J.; Ha, D. The AI Scientist: Towards Fully Automated Open-Ended Scientific Discovery. 2024, arXiv:2408.06292. arXiv.org e-Printarchive. https://arxiv.org/abs/2408.06292. acccessed August 12, 2024.
(42) Swan, M.; Kido, T.; Roland, E.; dos Santos, R. P. Math Agents: Computational Infrastructure, Mathematical Embedding, and Genomics. 2023, arXiv:2307.02502. arXiv.org e-Printarchive. https://arxiv.org/abs/2408.06292. acccessed July 04, 2023.
(43) Bran, A. M.; Cox, S.; Schilter, O.; Baldassari, C.; White, A. D.; Schwaller, P. Augmenting large language models with chemistry tools. *Nat. Mach. Intell.* **2024**, *6* (5), 525−535.
(44) Zhao, Z.; Wang, S.; Gu, J.; Zhu, Y.; Mei, L.; Zhuang, Z.; Cui, Z.; Wang, Q.; Shen, D. ChatCAD+: Toward a Universal and Reliable Interactive CAD Using LLMs. *IEEE Trans. Med. Imaging* **2024**, *43* (11), 3755−3766.
(45) Zheng, Z.; Rong, Z.; Rampal, N.; Borgs, C.; Chayes, J. T.; Yaghi, O. M. A GPT-4 Reticular Chemist for Guiding MOF Discovery. *Angew. Chem., Int. Ed.* **2023**, *62* (46), No. e202311983.
(46) Martell, A. E.; Hancock, R. D. *Metal Complexes in Aqueous Solutions*; Springer Science & Business Media, 2013.
(47) Irving, H.; Williams, R. J. P. 637. The stability of transition-metal complexes. *J. Chem. Soc.* **1953**, *0*, 3192−3210.
(48) Furukawa, H.; Cordova, K. E.; O'Keeffe, M.; Yaghi, O. M. The Chemistry and Applications of Metal-Organic Frameworks. *Science* **2013**, *341* (6149), No. 1230444.
(49) Daniel, M. C.; Astruc, D. Gold nanoparticles: Assembly, supramolecular chemistry, quantum-size-related properties, and applications toward biology, catalysis, and nanotechnology. *Chem. Rev.* **2004**, *104* (1), 293−346.

(50) Aricò, A. S.; Bruce, P.; Scrosati, B.; Tarascon, J. M.; Van Schalkwijk, W. Nanostructured materials for advanced energy conversion and storage devices. *Nat. Mater.* **2005**, *4* (5), 366−377.
(51) Yan, C.; Wang, T. A new view for nanoparticle assemblies: from crystalline to binary cooperative complementarity. *Chem. Soc. Rev.* **2017**, *46* (5), 1483−1509.
(52) Long, D.-L.; Tsunashima, R.; Cronin, L. Polyoxometalates: Building Blocks for Functional Nanoscale Systems. *Angew. Chem., Int. Ed.* **2010**, *49* (10), 1736−1758.
(53) Long, D.-L.; Burkholder, E.; Cronin, L. Polyoxometalate clusters, nanostructures and materials: From self assembly to designer materials and devices. *Chem. Soc. Rev.* **2007**, *36* (1), 105−121.
(54) Wang, Z.; Kononova, O.; Cruse, K.; He, T.; Huo, H.; Fei, Y.; Zeng, Y.; Sun, Y.; Cai, Z.; Sun, W.; Ceder, G. Dataset of solution-based inorganic materials synthesis procedures extracted from the scientific literature. *Sci. Data* **2022**, *9* (1), No. 231.
(55) Huang, C.-R.; Luo, X.; Chen, X.-G.; Song, X.-J.; Zhang, Z.-X.; Xiong, R.-G. A multiaxial lead-free two-dimensional organic-inorganic perovskite ferroelectric. *Natl. Sci. Rev.* **2021**, *8* (5), No. nwaa232.
(56) Zhang, J.; Wang, S.; Zhang, X.; Yao, Y.; Tian, R. One-step synthesis and characterization of copper aspirin. *Chem. Reagents* **2010**, *32* (03), 269−270.
(57) Manojlović-Muir, L. The crystal structure of copper(II) aspirinate. *Acta Crystallogr., Sect. B: Struct. Crystallogr. Cryst.* **1973**, *29* (10), 2033−2037.
(58) Cao, L.; Lin, Z.; Peng, F.; Wang, W.; Huang, R.; Wang, C.; Yan, J.; Liang, J.; Zhang, Z.; Zhang, T.; et al. Self-Supporting Metal−Organic Layers as Single-Site Solid Catalysts. *Angew. Chem., Int. Ed.* **2016**, *55* (16), 4962−4966.
(59) Turkevich, J.; Stevenson, P. C.; Hillier, J. A study of the nucleation and growth processes in the synthesis of colloidal gold. *Discuss. Faraday Soc.* **1951**, *11* (0), 55−75.
(60) Kimling, J.; Maier, M.; Okenve, B.; Kotaidis, V.; Ballot, H.; Plech, A. Turkevich Method for Gold Nanoparticle Synthesis Revisited. *J. Phys. Chem. B* **2006**, *110* (32), 15700−15707.
(61) Oliveira, A. E. F.; Pereira, A. C.; Resende, M. A. C.; Ferreira, L. F. Gold Nanoparticles: A Didactic Step-by-Step of the Synthesis Using the Turkevich Method, Mechanisms, and Characterizations. *Analytica* **2023**, *4* (2), 250−263.
(62) Jana, N. R.; Gearheart, L.; Murphy, C. J. Seed-Mediated Growth Approach for Shape-Controlled Synthesis of Spheroidal and Rod-like Gold Nanoparticles Using a Surfactant Template. *Adv. Mater.* **2001**, *13* (18), 1389−1393.
(63) Nikoobakht, B.; El-Sayed, M. A. Preparation and Growth Mechanism of Gold Nanorods (NRs) Using Seed-Mediated Growth Method. *Chem. Mater.* **2003**, *15* (10), 1957−1962.
(64) Tarnowicz-Staniak, N.; Vázquez-Díaz, S.; Pavlov, V.; Matczyszyn, K.; Grzelczak, M. Cellulose as an Inert Scaffold in Plasmon-Assisted Photoregeneration of Cofactor Molecules. *ACS Appl. Mater. Interfaces* **2020**, *12* (17), 19377−19383.
(65) Müller, A.; Das, S. K.; Fedin, V. P.; Krickemeyer, E.; Beugholt, C.; Bögge, H.; Schmidtmann, M.; Hauptfleisch, B. Rapid and Simple Isolation of the Crystalline Molybdenum-Blue Compounds with Discrete and Linked Nanosized Ring-Shaped Anions: $Na_{15}[Mo^{\{VI\}}_{\{126\}}Mo^{V}_{\{28\}}O_{462}H_{14}(H_2O)_{70}]_{0.5}$ $[Mo^{\{VI\}}_{\{124\}}Mo^{V}_{\{28\}}O_{457}H_{14}(H_2O)_{68}]_{0.5}$·ca. $400H_2O$ and $Na_{22}[Mo^{\{VI\}}_{\{118\}}Mo^{V}_{\{28\}}O_{442}H_{14}(H_2O)_{58}]$·ca. $250H_2O$. *Z. Anorg. Allg. Chem.* **1999**, *625* (7), 1187−1192.
(66) Müller, A.; Serain, C. Soluble Molybdenum Blues"des Pudels Kern". *Acc. Chem. Res.* **2000**, *33* (1), 2−10.
(67) Ma, X.; Zhang, C.; Hua, J.; Ma, P.; Wang, J.; Niu, J. A binuclear copper-substituted phosphomolybdate with reactive oxygen species catalytic ability and antimicrobial activity. *CrystEngComm* **2019**, *21* (3), 394−398.
(68) Zhang, C.; Zhang, M.; Shi, H.; Zeng, Q.; Zhang, D.; Zhao, Y.; Wang, Y.; Ma, P.; Wang, J.; Niu, J. A high-nuclearity isopolyoxotungstate based manganese cluster: one-pot synthesis and step-by-step assembly. *Chem. Commun.* **2018**, *54* (43), 5458−5461.
(69) Zhang, M.; Liu, B.; Zhang, H.; Zhang, C.; Wang, J.; Niu, J. Synthesis and Mechanism Studies of a High-Nuclear $Mn_{72}W_{48}$ Cluster. *Inorg. Chem.* **2020**, *59* (18), 13733−13740.
(70) Zhang, Z.-M.; Yao, S.; Li, Y.-G.; Wu, H.-H.; Wang, Y.-H.; Rouzières, M.; Clérac, R.; Su, Z.-M.; Wang, E.-B. A polyoxometalate-based single-molecule magnet with a mixed-valent $\{Mn^{IV}_2Mn^{III}_6Mn^{II}_4\}$ core. *Chem. Commun.* **2013**, *49* (25), 2515−2517.
(71) Bassil, B. S.; Ibrahim, M.; Al-Oweini, R.; Asano, M.; Wang, Z.; van Tol, J.; Dalal, N. S.; Choi, K.-Y.; Ngo Biboum, R.; Keita, B.; et al. A Planar $\{Mn_{19}(OH)_{12}\}^{26+}$ Unit Incorporated in a 60-Tungsto-6-Silicate Polyanion. *Angew. Chem., Int. Ed.* **2011**, *50* (26), 5961−5964.
(72) Pohl, I. A. M.; Westin, L. G.; Kritikos, M. Preparation, Structure, and Properties of a New Giant Manganese Oxo-Alkoxide Wheel, $[Mn_{19}O_{12}(OC_2H_4OCH_3)_{14}(HOC_2H_4OCH_3)_{10}]\cdot HOC_2H_4OCH_3$. *Chem. - Eur. J.* **2001**, *7* (16), 3438−3445.
(73) Deng, Y.-K.; Su, H.-F.; Xu, J.-H.; Wang, W.-G.; Kurmoo, M.; Lin, S.-C.; Tan, Y.-Z.; Jia, J.; Sun, D.; Zheng, L.-S. Hierarchical Assembly of a $\{Mn^{II}_{15}Mn^{III}_4\}$ Brucite Disc: Step-by-Step Formation and Ferrimagnetism. *J. Am. Chem. Soc.* **2016**, *138* (4), 1328−1334.
(74) Brockman, J. T.; Huffman, J. C.; Christou, G. A High Nuclearity, Mixed-Valence Manganese(III,IV) Complex: $[Mn_{21}O_{24}(OMe)_8(O_2CCH_2tBu)_{16}(H_2O)_{10}]$. *Angew. Chem., Int. Ed.* **2002**, *41* (14), 2506−2508.
(75) Lis, T. Preparation, structure, and magnetic properties of a dodecanuclear mixed-valence manganese carboxylate. *Acta Crystallogr., Sect. B: Struct. Crystallogr. Cryst.* **1980**, *36* (9), 2042−2046.
(76) McKay, M. D.; Beckman, R. J.; Conover, W. J. A Comparison of Three Methods for Selecting Values of Input Variables in the Analysis of Output from a Computer Code. *Technometrics* **1979**, *21* (2), 239−245.
(77) Nomiya, K.; Takahashi, T.; Shirai, T.; Miwa, M. Anderson-type heteropolyanions of molybdenum(VI) and tungsten(VI). *Polyhedron* **1987**, *6* (2), 213−218.

https://doi.org/10.1021/jacs.5c05916
J. Am. Chem. Soc. 2025, 147, 23014−23025